Nanoscale

PAPER

View Article Online
View Journal

Cite this: DOI: 10.1039/d6nr00929h

Influence of composition–phase interplay on the electrochemical activity of ternary transition metal dichalcogenides

Manoj Palabathuni, Niraj Nitish Patil, Suvodeep Sen, Geetu Kumari, Sarah Guerin and Shalini Singh *

Received 6th March 2026,
Accepted 29th April 2026

DOI: 10.1039/d6nr00929h

rsc.li/nanoscale

Alloying is a powerful strategy to tailor the electronic structures of 2D transition metal dichalcogenides. Controlling the functionalities is essential to explore the full potential of these ternary nanosheets with tunable electronic properties. Here, Nb was successfully alloyed with W to form ternary $Nb_xW_{1-x}S_2$ nanosheets with different stoichiometric ratios *via* colloidal hot-injection synthesis. Incorporation of Nb alters the band structure of parent WS_2, allowing for controlled tuning of electronic properties. High resolution transmission electron microscopy reveals an irregular atomic arrangement at higher Nb concentrations, with a notable transition from the pure 2H phase to a mixed 2H–1T′ phase at a controlled concentration of Nb content in the composition. Nb induces a shift of the Fermi level, causing a transition from semiconducting to metallic nature in ternary nanosheets, which facilitates enhanced electrocatalytic activity for the hydrogen evolution reaction (HER) of $Nb_{0.5}W_{0.5}S_2$ compared to pristine WS_2.

Introduction

Transition metal dichalcogenides (TMDs) are fascinating materials due to their intriguing properties with promising applications in energy conversion and storage.[1,2] In the post-graphene era, exploration of atomically thin TMDs has accelerated, driven by their layered morphology with remarkable anisotropic physical and electronic properties.[3,4] The rich phase diagram of these layered materials offers distinctive characteristics, such as tunable bandgap, phase dependent conductivity and high carrier mobility.[5–7] In addition, their large surface area, accessible interlayer spacing and unique electronic properties make TMDs particularly attractive for electrocatalytic applications.[8,9]

The electronic properties of TMDs are predominantly determined by their versatile chemical compositions and structural phases. Thus, achieving their full functional potential necessitates deliberate regulation of those electronic properties as a fundamental prerequisite. Unlike most binary TMDs, their tailored ternary counterparts offer an additional degree of control for tailoring electronic and surface properties.[10–12] The judicious incorporation of dopants not only expands the structural landscape but also introduces new pathways for electronic modulation.[13] Specifically, depending on the choice of metal/chalcogen and their crystal structure, the different localization of atomic d orbitals arising due to the introduction of a third/fourth element is crucial for spatial delocalization of their discrete energy levels. At higher dopant concentrations, this effect results in band gap modification and redistribution of the density of states (DOS).[14] Moreover, the intrinsic reduced dimensionality of 2D TMDs further amplifies the effectiveness of such dopant-induced band structure engineering. For instance, bandgap engineering has been well explored in multielement compositions such as $MoS_{2(1-x)}Se_{2x}$, $WS_{2x}Se_{2(1-x)}$, $Mo_{1-x}W_xS_2$, $ReS_{2x}Se_{2(1-x)}$, and $Mo_xW_{1-x}S_{2y}Se_{2(1-y)}$, by tuning the chemical composition of metal cations and chalcogen anions.[15–19]

To date, a wide range of metals have been incorporated into WS_2 to tailor its electronic and catalytic properties.[9,20] Early transition metals such as V and Ta can effectively modulate the carrier concentration. However, their incorporation often induces structural instability. In contrast, late transition metals, *e.g.*, Fe, Co, and Ni, tend to form secondary phases rather than true substitutional alloys.[21] In this context, Nb has emerged as one of the effective and widely reported dopant/alloying elements for WS_2. Owing to its close atomic size and strong electronic compatibility with W, Nb can be stably incorporated into the WS_2 lattice without disrupting the crystal structure. Also, Nb substitution induces controlled p-type doping and optimizes the local electronic environment, directly regulating charge transfer and hydrogen adsorption energies.[22–24] Despite these advantages, most ternary and qua-

Department of Chemical Sciences and Bernal Institute, University of Limerick, Ireland. E-mail: shalini.singh@ul.ie

ternary compositions of TMDs, including Nb-substituted WS_2, have been synthesized by using chemical vapour deposition (CVD).[25,26] While CVD enables substitution levels exceeding 10% and has demonstrated a clear n- to p-type crossover with metal atoms acting as electron acceptors, the process requires high growth temperatures (>800 °C).[27] Such elevated temperatures introduce significant issues in precursor reactivity and volatility, often leading to poor compositional control, inhomogeneous alloying and binary phase separation. These limitations restrict kinetic tunability and hinder the rational design and adoption of these materials in practical applications. Therefore, the design of a general and controllable synthetic strategy remains critical. Compared to high temperature synthesis techniques, the colloidal hot injection synthesis route offers a low temperature chemical route that enables precise stoichiometric control and homogeneous alloying. This synthetic flexibility enables the tunability of the band structures and systematic modulation of electronic properties.[28,29]

In this study, we report a low-temperature colloidal hot-injection strategy for controlled incorporation of Nb into WS_2 nanosheets enabling the synthesis of ternary $Nb_xW_{1-x}S_2$ over a wide compositional range with precise control of metal stoichiometry. Across all compositions, the experimentally determined metal ratios closely matched the nominal stoichiometry defined by the starting precursor, confirming reliable compositional control. Structural analysis by high-resolution transmission electron microscopy (HRTEM) reveals the composition dependent crystal phase evolution and defect formation induced by Nb substitution, while X-ray photoelectron spectroscopy (XPS) further evidences the corresponding phase transitions. In addition, XPS analysis indicates the formation of sulfur vacancies, and valence band spectra show that increasing Nb content modifies the electronic structures, leading to band restructuring and a reduced bandgap. These coupled structural and electronic modifications lead to a significant enhancement of the electrocatalytic hydrogen evolution reaction (HER) activity of the nanosheets with a mixed phase composition (x = 0.5) in acidic electrolyte. The improved activity is attributed to the increased density of catalytically active sites arising from sulfur vacancies and enhanced charge transfer enabled by Nb-induced band modulation.

Results and discussion

$Nb_xW_{1-x}S_2$ nanostructures were synthesised *via* the hot-injection colloidal route using a pre-mixed stock dispersion $W(CO)_6$, $NbCl_5$ and S powder in OLA. The molar ratio of Nb and W precursors in the stock dispersion was adjusted while maintaining the stock volume constant (as given in Table S1, SI). This stock was injected into a coordinating ligand–solvent mixture at 300 °C and allowed to react for 120 min. Here, the precursor selectivity was critical in achieving controlled Nb substitution within the WS_2 lattice. For instance, use of WCl_6 as a W source led to the formation of oxide by-products and particles enriched in W, Nb, O and Cl as revealed by XRD and elemental mapping (Fig. S1 and 2), even under inert con-

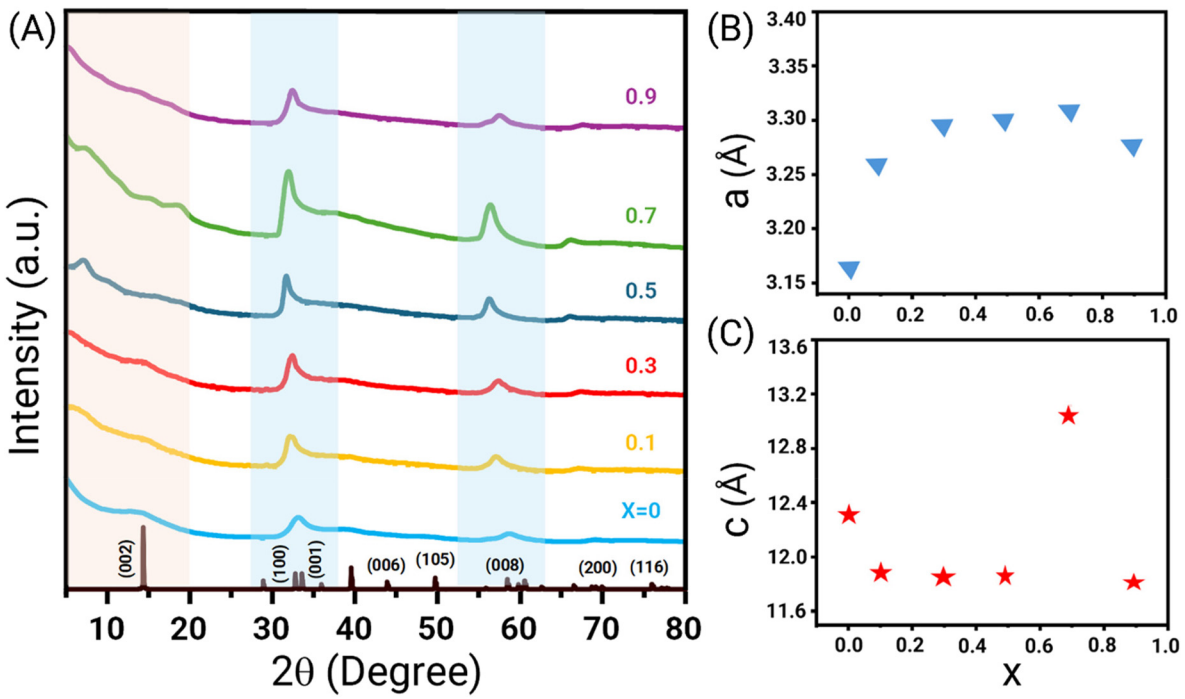

Fig. 1 (A) XRD patterns of $W_{1-x}Nb_xS_2$ (x = 0 to 0.9); shaded regions highlight the shift in diffraction planes. (B) Lattice constant *a*. (C) Lattice constant *c*.

ditions, reflecting the high oxophilicity of WCl_6.[30] In contrast, $W(CO)_6$ undergoes thermal decomposition to generate metallic W while simultaneously acting as an *in situ* reducing agent.[31,32] The resulting reductive environment stabilizes lower Nb oxidation states, thereby facilitating Nb incorporation into WS_2 and promoting ternary phase formation while suppressing Nb oxide impurities in the reaction flask. Moreover, this $W(CO)_6$ based synthesis protocol affords a chemical yield of ~75% (see SI Table S2 for yield calculations), underscoring the efficiency and sustainability of this approach.

The powder X-ray diffraction (XRD) patterns for all ternary compositions are shown in Fig. 1A. Peaks corresponding to $x = 0$ represent the 2H phase WS_2 with lattice constants a = 3.18 Å and c = 12.5 Å, referenced to the JCPDS: 04-016-3255; $P6_3/mmc$. Highlighted regions show systematic shifts in (002), (100), (110) and (200) peaks with the gradual increase in x. Compositions with x ranging from 0.1 to 0.5 show a linear shift towards lower 2θ angles, which signifies the progressive lattice expansion with increasing Nb in the samples. This is further corroborated by the a and c lattice constants (shown in Fig. 1(B and C)) that are derived from the peak positions of (100) and (008). The in-plane lattice parameters (a) expand from 3.16 Å ($x = 0$) to 3.29 Å ($x = 0.5$) due to a larger ionic radius of Nb^{5+} (~0.64 Å) compared to that of W^{6+} (~0.60 Å).[33] Simultaneously, the out-of-plane parameter (c) contracts from 12.3 Å ($x = 0$) to 11.85 Å ($x = 0.5$), likely due to the stronger Nb–S bonding and reduced interlayer spacing.[34] However, a deviation from the trend was observed in the samples with $x = 0.7$ and 0.9, which could be attributed to the non-homogeneous mixing of atoms in the lattice. To ensure that the phase remains unchanged, XRD patterns of the sample ($x = 0.5$) were recorded before and after annealing at 400 °C. There is no change in the peak position and intensities observed, indicating that the crystal structure and phase composition remain intact (Fig. S3).

Transmission electron microscopy (TEM) images of $Nb_xW_{1-x}S_2$ (x = 0, 0.1, 0.3 and 0.7) with insets of histograms are shown in Fig. 2A. The side view (of sample, $x = 0.5$) high-resolution TEM image confirms abundant exposed edges shown in Fig. 2B with an interlayer spacing of 0.7 nm (Fig. S4). The elemental mapping was obtained using Energy-Dispersive X-Ray Spectroscopy (EDS) for the $x = 0.5$ sample (Fig. 2C), confirming the homogeneous distribution of W, Nb and S. The results of the remaining samples (x = 0.1, 0.3, 0.7) are given in Fig. S5. The stoichiometric ratios of elements in all samples

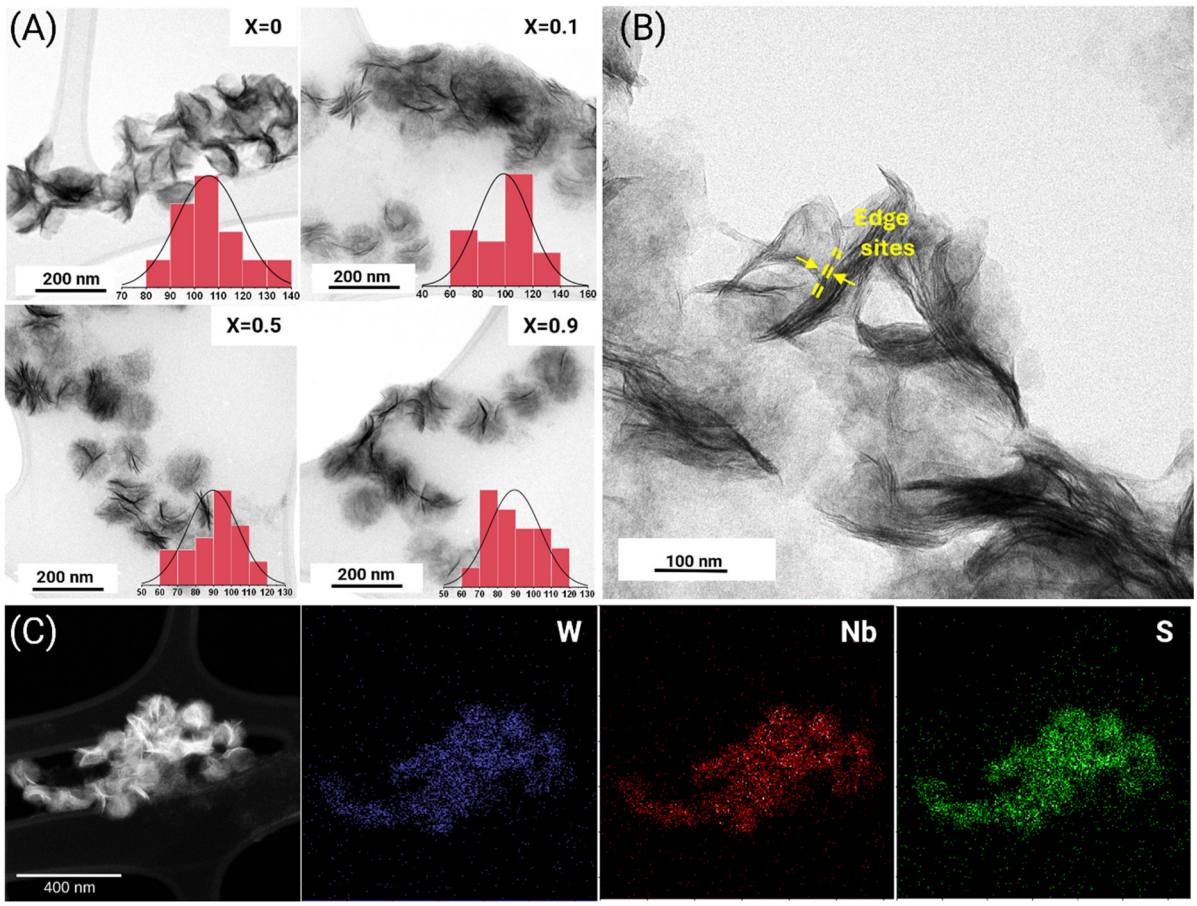

Fig. 2 (A) TEM images of $W_{1-x}Nb_xS_2$ (x = 0, 0.1, 0.5 and 0.9) each with an inset histogram, showing the corresponding nanosheet distribution and average size. (B) Enlarged TEM image of $x = 0.5$. (C) STEM ($x = 0.5$) and elemental mapping showing the spatial distribution of W, Nb and S, confirming the uniform elemental dispersion across the nanosheets.

were confirmed by X-ray photoelectron spectroscopy (XPS) and inductively coupled plasma atomic emission spectroscopy (ICP-OES) (Table S1). The data indicate that the atomic ratios of metals were almost the same as those of the precursors [W$(CO)_6$] : [$NbCl_5$] reflecting positively on the chemical yield of the synthetic approach. The ratio of [S]/[W] + [Nb] is close to 2 for samples with $x \leq 0.7$, suggesting that the S vacancies are negligible. However, this ratio decreases at higher x values, indicating sulfur vacancy formation at higher Nb content, as is evident from the XPS and SEM–EDS spectra (supporting Fig. S6–8).

HRTEM analysis of $Nb_xW_{1-x}S_2$ nanosheets was performed to investigate the structural impact of Nb substitution. Interestingly, the analysis revealed phase transition in the ternary composition. Fig. 3A and B provide an overview of 2H and 1T′ crystal structures, which are known polymorphs of WS_2. The 2H phase exhibits a trigonal prismatic coordination with hexagonal symmetry, while the 1T′ phase shows a distorted octahedral coordination with metallic behaviour. The HRTEM image of WS_2 shows the arrangement of W and S in a hexagonal ring pattern matched with the overlaid ball-and-stick model of H-phase WS_2 nanosheets (x = 0), shown in Fig. 3C, consistent with the hexagonal symmetry of the 2H phase, including an interplanar spacing ($d_{(100)}$ = 0.27 nm).

When $x \geq 0.1$, the coexistence of both 2H and 1T′ phases is observed, as shown in Fig. 3D, indicating that Nb alloying induces the partial phase transition. The highlighted yellow region shows 2H and 1T′ phases with an enlarged HRTEM image on the left. The observed interplanar spacing of 0.27 nm for the (010) plane in 2H and the (100) plane in 1T′ supports the presence of mixed phase domains resulting from substitution of Nb at x = 0. Beyond x > 0.1, we observed severe lattice irregularities, with disrupted fringes and unclear periodicity in several regions, as shown in Fig. S9. Thus, it confirms that higher concentrations of x destabilize the pristine 2H lattice, promoting mixed phase and defect formation within the nanosheets. However, such irregularities are commonly associated with electrocatalytic activity, as they serve as active sites for electrocatalysis.

XPS analysis of $Nb_xW_{1-x}S_2$ shown in Fig. 4 reveals a distinct shift in binding energies, indicating changes in the electronic properties due to Nb incorporation. The deconvoluted spectra of W 4f and Nb 3d confirm the presence of different oxidation states, suggesting charge distribution when x > 0. A clear sign

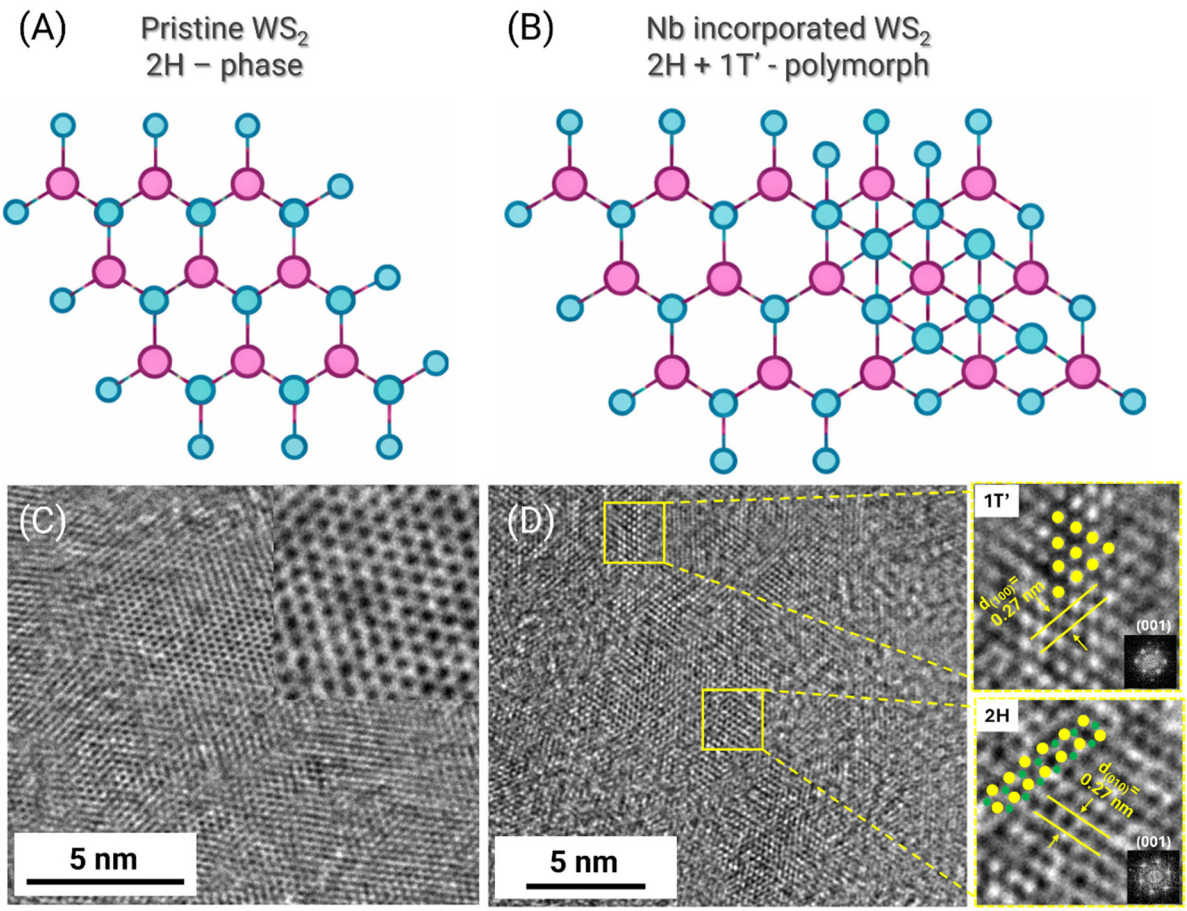

Fig. 3 Ball-and-stick models illustrate the crystal structures of (A) 2H and (B) 2H–1T′ phases. HRTEM image of $Nb_xW_{1-x}S_2$ NSs (C) at x = 0, with an enlarged inset, and (D) x = 0.1, where the yellow highlight indicates (2H) and (1T′) regions. Enlarged views of the highlighted areas are shown on the right side. The 2H and 1T′ atomic arrangements are shown in yellow and green dots.

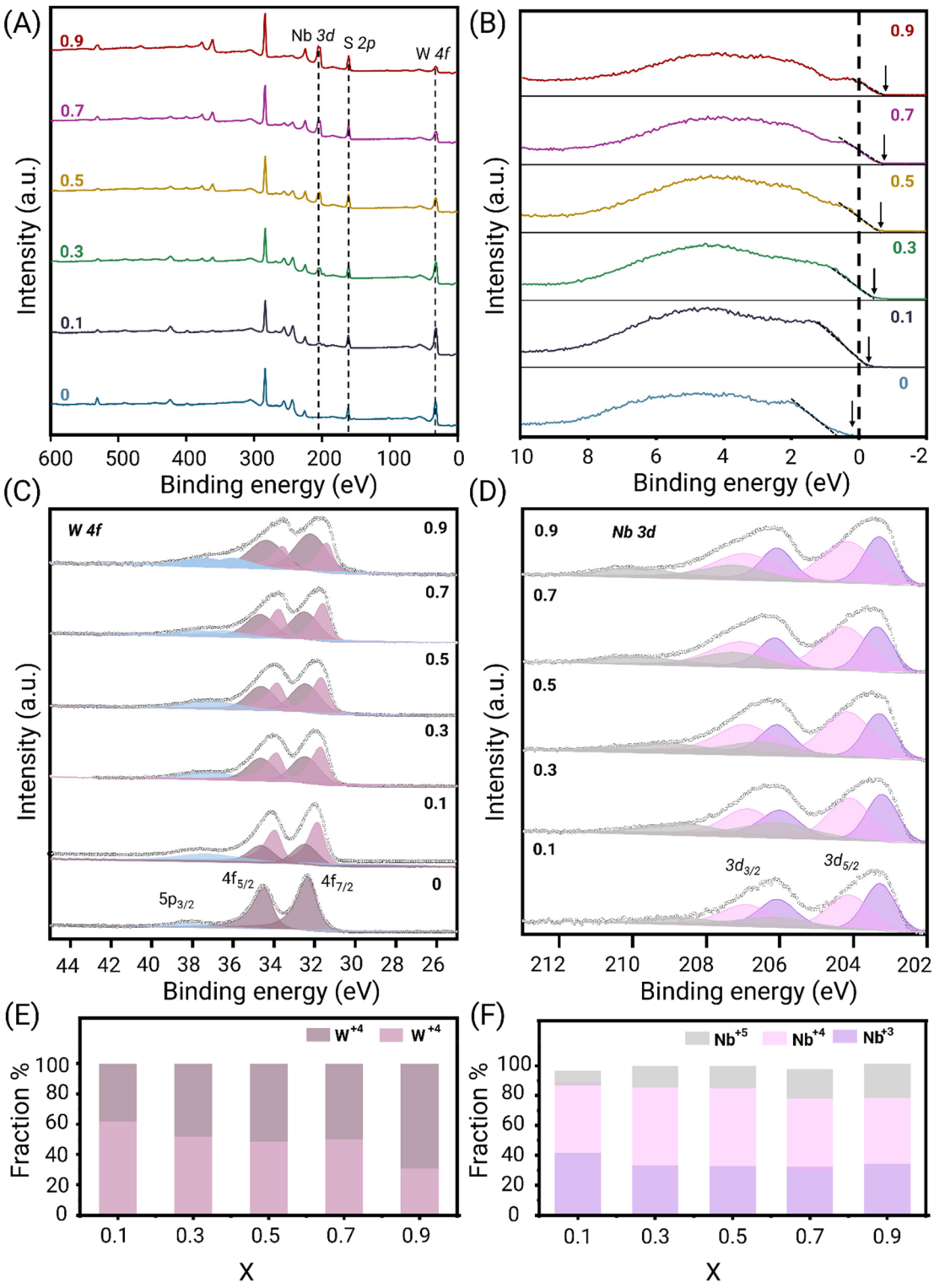

Fig. 4 (A) XPS survey scan of $Nb_xW_{1-x}S_2$ confirming the presence of W, Nb and S. (B) VBS at $x \geq 0$. High-resolution XPS peaks of (C) W-$4f_{7/2}$ and $4f_{5/2}$, (D) Nb-$3d_{5/2}$ and $3d_{3/2}$. Fractional percentages of (E) Nb and (F) W oxidation states *vs.* x obtained by deconvolution of Nb 3d and W 4f peaks, respectively.

of composition tuning is shown in the survey scan (Fig. 4A), where the W 4f peak intensity decreases with increasing x, while the Nb 3d peak intensity increases. Valance band spectroscopy (VBS) of all the compositions reveals the valence band maximum (VBM) Fermi energy level (E_F) as shown in Fig. 4B. The VBM appeared for pristine WS_2 (≥0 eV) and (<0 eV) for all

ternary compositions. As the Nb content increases, the downshift of the metal d-states relative to the Fermi level occurs, suggesting a decrease in the d-band center (ε_d).[35] This indicates that the Nb content induces a semiconductor to metallic behaviour transition, which is further supported by the W 4f spectra analysis as discussed below.

Two characteristic peaks of W were observed (Fig. 4C) – W $4f_{7/2}$ at 32.3 eV and $4f_{5/2}$ at 34.5 eV. In WS_2, the $4f_{7/2}$ peak at 32.3 eV (blue-shifted from neutral W at 31.2 eV) is attributed to the naturally occurring semiconductive 2H phase (W–S binding structures). However, the deconvolution of compositions with $x \geq 0.1$ reveals two additional peaks at 31.8 eV and

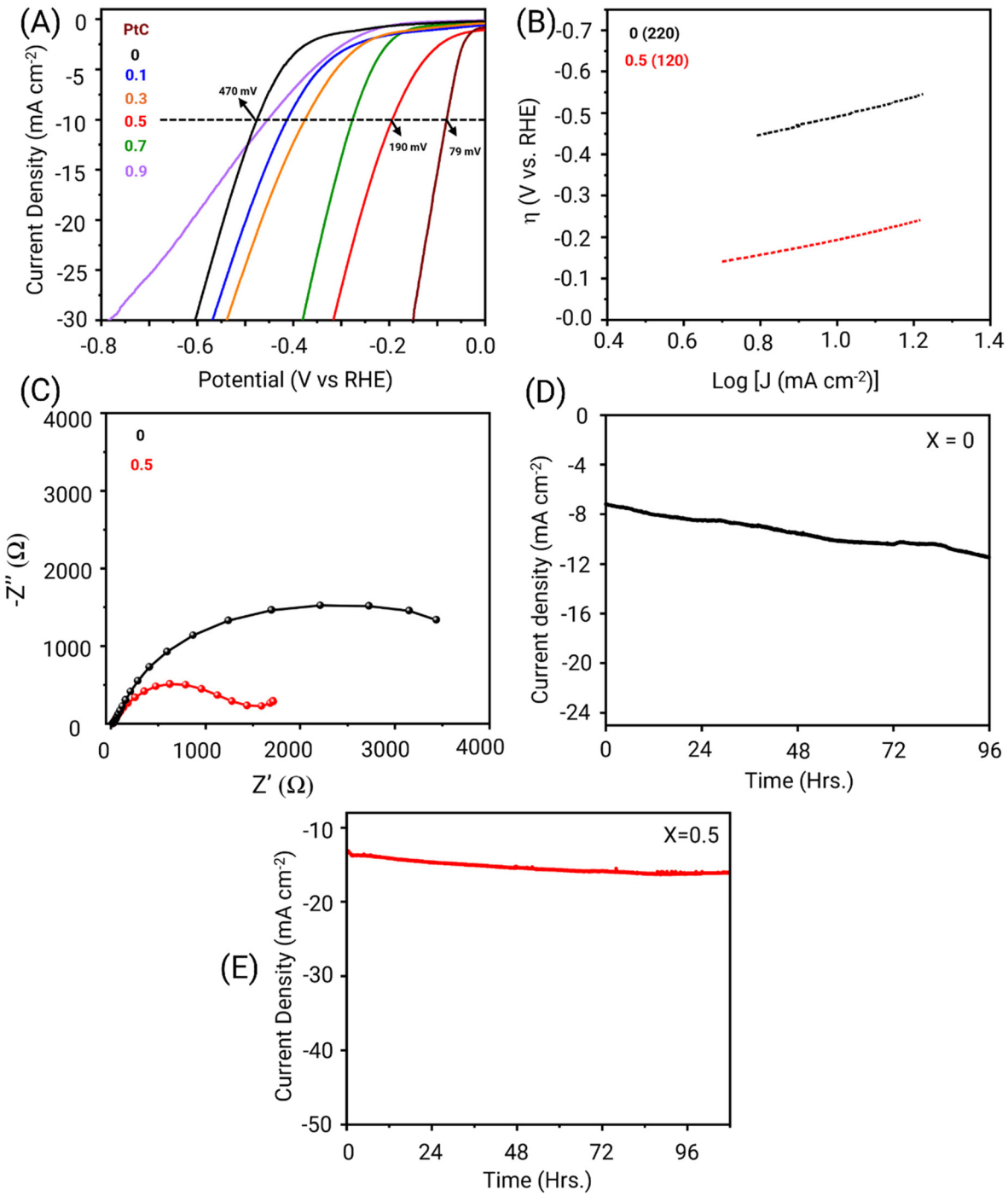

Fig. 5 HER performance of $Nb_xW_{1-x}S_2$ ternary nanosheets (current density and overpotential at 10 mA cm^{-2}). (A) Polarization curves obtained with a scan rate of 2 mV s^{-1}, (B) corresponding slopes, (C) Nyquist plot from Electrochemical Impedance Spectroscopy (EIS). Chronoamperometric stability of samples: (D) x = 0 at −0.470 V and (E) x = 0.5 at −0.190 V.

33.9 eV, corresponding to the 1T′ phase, as already discussed in the HRTEM analysis above.[36] The extra electrons introduced by Nb destabilize the pure semiconducting structure and initiate a 2H → 1T′ phase transition. The new peaks of the 1T′ phase show a decrease in binding energies as the Nb concentration increases. This could be observed owing to the shift in Fermi levels caused by increased density of d-orbital electrons. Similarly, the deconvolution of the Nb $3d_{5/2}$ peak shown in Fig. 4D indicates Nb^{3+}, Nb^{4+}, and Nb^{5+} states at 203.3, 204.1, and 206.1 eV respectively.

The variations in oxidation states of W and Nb (as shown in Fig. 4E and F), deconvoluted from the W $4f_{7/2}$ and Nb $3d_{5/2}$ peaks across all the composition, are presented. Despite phase coexistence, W remains entirely consistent in the +4 oxidation state. In contrast, Nb is present in Nb^{3+}, Nb^{4+} and Nb^{5+} ion states. The Nb^{5+} state originates from Nb–O bonding and its fraction increases, suggesting electron depletion by W ions along with increased surface oxidation,[37] whereas the Nb^{3+} and Nb^{4+} states originated from the Nb–S bonding structure. The reducing environment created by the decomposition of $W(CO)_6$ helps stabilize these lower oxidation states, while restricting fully the formation of Nb oxide species at Nb^{5+} states.

Electrocatalytic HER

The electrocatalytic HER performance of $Nb_xW_{1-x}S_2$ was evaluated in the acidic electrolyte (0.5 M H_2SO_4). Fig. 5A shows the linear sweep voltammetry (LSV) using the applied potentials *vs.* reversible hydrogen electrode (RHE), which is equal to the overpotentials (η). $\eta_{J=10}$ denotes the η value at J = 10 mA cm^{-2}. Among all ternary compositions, the x = 0.5 composition exhibits the lowest overpotential values such as 190 mV. The Tafel slope shown in Fig. 5B, which was obtained from linear fitting of the low potential region, is 120 mV dec^{-1} for x = 0.5. In comparison, the commercial 20 wt% Pt/C catalyst as a reference sample exhibited $\eta_{J=10}$ = 79 mV.

Fig. 5A illustrates the composition dependence of the HER performance, with the maximum performance observed for the x = 0.5 sample. This composition activity is superior to that of the various previously reported modified TMD systems including those prepared based on doping, alloying, and heterostructure engineering, as summarized in Table S3. In support of the LSV data, the EIS data in Fig. 5C demonstrate a comparable composition-dependent behaviour, highlighting the pivotal role of charge transfer resistance (R_{CT}) in determining performance. The fitted charge-transfer resistance (R_{CT}) for the sample exhibiting the best HER performance (x = 0.5) is 157 Ω, whereas it is 1530 Ω for WS_2. The results indicate that transfer kinetics are significantly improved in the (x = 0.5) sample. Long-term chronoamperometry (Fig. 5D and E) shows that, unlike the x = 0 sample, the x = 0.5 sample maintained stable current for nearly 100 h.

Substituting Nb, induces a semiconductor to semi metallic transition, as confirmed by the shift of the valence band maximum in the XPS. We observed increased HER performance for x = 0.5, highlighting the importance of optimizing Nb for improved HER activity. For x = 0.5, the Nb concentration likely enhanced the electrical conductivity, as confirmed by the EIS analysis and simultaneously increased the HER active sites. However, higher concentrations of Nb deteriorate the performance. This can be due to excessive structural distortion or defect formation that hinders electron transfer, increasing the overpotentials and slowing down the reaction kinetics. On the other hand, with increasing x, the formation of oxide species becomes more pronounced (evidence from XPS data supports the observation), which negatively impacts the electrocatalytic performance by increasing the charge transfer resistance and reducing the availability of H^+ absorption sites. The results demonstrate that a carefully optimized ternary composition is crucial for achieving the best HER performance in acidic media, as balance between conductivity, structural distortions and active sites governs the overall catalytic efficiency.

Conclusion

In summary, we successfully synthesized ternary alloy nanosheets *via* a colloidal hot injection technique, demonstrating the critical role of precursor selectivity. Fully tunable control over composition was achieved, enabling systematic modulation of their structural and electronic properties. The uniform nanosheet morphology with accurate Nb stoichiometries was confirmed by XPS, ICP, and SEM-EDX. TEM revealed a transition from pure 2H to a coexistence of 2H and 1T′ at x = 0.1, and further increases in concentration ($x \geq 0.3$) induced more defect formation and irregular arrangement in the lattice. The oxidation became more significant at higher x, which hindered the catalytic activity, and alloy nanosheets at x = 0.5 showed exceptional HER activity with η = 190 mV (at J = 10 mA cm^{-2}) and demonstrated a remarkable stability over 100 h at −0.2 V. In support, the XPS-derived VBM indicates band restructuring and Fermi level shifts, collectively contributing to exceptional HER activity. Our study highlights how stoichiometric engineering can effectively tailor the structural and electronic properties of 2D TMDs. These insights provide a rational basis for designing next generation earth abundant electrocatalysts for sustainable energy conversion.

Conflicts of interest

The authors declare no competing financial interest.

Data availability

The data that support the findings of this study are available on request from the corresponding author.

Supplementary information (SI): materials and methods for the synthesis of nanostructures with additional data obtained from: (i) XRD analysis, (ii) ICP-OES analysis, (iii) STEM-EDX analysis, (iv) SEM – EDS spectral analysis for stoichiometric ratios, (v) HRTEM analysis – for lattice distortions or defect for-

mation, and (vi) XPS spectral analysis. See DOI: https://doi.org/10.1039/d6nr00929h.

Acknowledgements

This publication has emanated from research conducted with financial support from Taighde Éireann – Research Ireland under Grant Number 22/FFP-P/11591. M. P. acknowledges IRC (GOIPG/2024/3075) for funding. N. N. P. acknowledges funding from AMBER (12/rc/2278_p2). S. S. acknowledges the Horizon TMA MSCA Postdoctoral Fellowship (Project ID 101207456).

References

1 S. Gupta, J.-J. Zhang, J. Lei, H. Yu, M. Liu, X. Zou and B. I. Yakobson, Two-Dimensional Transition Metal Dichalcogenides: A Theory and Simulation Perspective, *Chem. Rev.*, 2025, **125**(2), 786–834, DOI: 10.1021/acs.chemrev.4c00628.

2 S. Roy, A. Joseph, X. Zhang, S. Bhattacharyya, A. B. Puthirath, A. Biswas, C. S. Tiwary, R. Vajtai and P. M. Ajayan, Engineered Two-Dimensional Transition Metal Dichalcogenides for Energy Conversion and Storage, *Chem. Rev.*, 2024, **124**(16), 9376–9456, DOI: 10.1021/acs.chemrev.3c00937.

3 A. Gupta, T. Sakthivel and S. Seal, Recent Development in 2D Materials beyond Graphene, *Prog. Mater. Sci.*, 2015, **73**, 44–126, DOI: 10.1016/j.pmatsci.2015.02.002.

4 S. Manzeli, D. Ovchinnikov, D. Pasquier, O. V. Yazyev and A. Kis, 2D Transition Metal Dichalcogenides, *Nat. Rev. Mater.*, 2017, **2**(8), 17033, DOI: 10.1038/natrevmats.2017.33.

5 *Bandgap engineering of two-dimensional semiconductor materials | npj 2D Materials and Applications*. https://www.nature.com/articles/s41699-020-00162-4 (accessed 2026-02-23).

6 Q. Fu, J. Han, X. Wang, P. Xu, T. Yao, J. Zhong, W. Zhong, S. Liu, T. Gao, Z. Zhang, L. Xu and B. Song, 2D Transition Metal Dichalcogenides: Design, Modulation, and Challenges in Electrocatalysis, *Adv. Mater.*, 2021, **33**(6), 1907818, DOI: 10.1002/adma.201907818.

7 X. Chia and M. Pumera, Characteristics and Performance of Two-Dimensional Materials for Electrocatalysis, *Nat. Catal.*, 2018, **1**(12), 909–921, DOI: 10.1038/s41929-018-0181-7.

8 N. Kapuria, N. N. Patil, K. M. Ryan and S. Singh, Two-Dimensional Copper Based Colloidal Nanocrystals: Synthesis and Applications, *Nanoscale*, 2022, **14**(8), 2885–2914, DOI: 10.1039/D1NR06990J.

9 P. Zhou, P. Schiettecatte, M. Vandichel, A. Rousaki, P. Vandenabeele, Z. Hens and S. Singh, Synthesis of Colloidal WSe2 Nanocrystals: Polymorphism Control by Precursor-Ligand Chemistry, *Cryst. Growth Des.*, 2021, **21**(3), 1451–1460, DOI: 10.1021/acs.cgd.0c01036.

10 X.-M. Pham, N. N. Patil, S. A. Ahad, N. Kapuria, K. A. Owusu, H. Geaney, S. Singh and K. M. Ryan, Electrophoretic Assisted Fabrication of Additive-Free WS2 Nanosheet Anodes for High Energy Density Lithium-Ion Batteries, *Nanoscale*, 2024, **16**(44), 20496–20504, DOI: 10.1039/D4NR03025G.

11 D. Mastrippolito, A. Shahmanesh, M. Cavallo, E. Bossavit, I. L. E. Abed, C. Dabard, S. Singh, M. G. Silly, F. Capitani, N. Peric, L. Biadala, A. Zitolo, J. Avila, F. Carlà, C. Tresca, E. Lhuillier, B. Mahler and D. Pierucci, In Situ Investigation of 1T′/1H Phase Transition in Colloidal WS2 Monolayers, *Nanoscale*, 2025, **17**(43), 25174–25186, DOI: 10.1039/D5NR03092G.

12 H. Zhang, Ultrathin Two-Dimensional Nanomaterials, *ACS Nano*, 2015, **9**(10), 9451–9469, DOI: 10.1021/acsnano.5b05040.

13 S. E. Muller, M. P. Prange, Z. Lu, W. S. Rosenthal and J. A. Bilbrey, An Open Database of Computed Bulk Ternary Transition Metal Dichalcogenides, *Sci. Data*, 2023, **10**(1), 336, DOI: 10.1038/s41597-023-02103-4.

14 J. H. Kim, H. Sung and G.-H. Lee, Phase Engineering of Two-Dimensional Transition Metal Dichalcogenides, *Small Sci.*, 2024, **4**(1), 2300093, DOI: 10.1002/smsc.202300093.

15 F. Cui, Q. Feng, J. Hong, R. Wang, Y. Bai, X. Li, D. Liu, Y. Zhou, X. Liang, X. He, Z. Zhang, S. Liu, Z. Lei, Z. Liu, T. Zhai and H. Xu, Synthesis of Large-Size 1T′ ReS2xSe2(1−x) Alloy Monolayer with Tunable Bandgap and Carrier Type, *Adv. Mater.*, 2017, **29**(46), 1705015, DOI: 10.1002/adma.201705015.

16 H. S. Kang, J. H. Kang, S. Lee, K. Lee, D. H. Koo, Y.-S. Kim, Y. J. Hong, Y.-J. Kim, K. Kim, D. Lee and C.-H. Lee, Bowing-Alleviated Continuous Bandgap Engineering of Wafer-Scale WS2xSe2(1-x) Monolayer Alloys and Their Assembly into Hetero-Multilayers, *NPG Asia Mater.*, 2022, **14**(1), 90, DOI: 10.1038/s41427-022-00437-w.

17 S. Susarla, A. Kutana, J. A. Hachtel, V. Kochat, A. Apte, R. Vajtai, J. C. Idrobo, B. I. Yakobson, C. S. Tiwary and P. M. Ajayan, Quaternary 2D Transition Metal Dichalcogenides (TMDs) with Tunable Bandgap, *Adv. Mater.*, 2017, **29**(35), 1702457, DOI: 10.1002/adma.201702457.

18 Q. Feng, N. Mao, J. Wu, H. Xu, C. Wang, J. Zhang and L. Xie, Growth of MoS2(1−x)Se2x (x = 0.41–1.00) Monolayer Alloys with Controlled Morphology by Physical Vapor Deposition, *ACS Nano*, 2015, **9**(7), 7450–7455, DOI: 10.1021/acsnano.5b02506.

19 Z. Wang, P. Liu, Y. Ito, S. Ning, Y. Tan, T. Fujita, A. Hirata and M. Chen, Chemical Vapor Deposition of Monolayer Mo1−xWxS2 Crystals with Tunable Band Gaps, *Sci. Rep.*, 2016, **6**(1), 21536, DOI: 10.1038/srep21536.

20 T. F. Jaramillo, K. P. Jørgensen, J. Bonde, J. H. Nielsen, S. Horch and I. Chorkendorff, Identification of Active Edge Sites for Electrochemical H2 Evolution from MoS2 Nanocatalysts, *Science*, 2007, **317**(5834), 100–102, DOI: 10.1126/science.1141483.

21 Y. Yang, X.-L. Fan, R. Pan and W.-J. Guo, First-Principles Investigations of Transition-Metal Doped Bilayer WS2,

Phys. Chem. Chem. Phys., 2016, **18**(15), 10152–10157, DOI: 10.1039/C6CP00701E.

22 X. Wu, H. Zhang, J. Zhang and X. W. Lou, Recent Advances on Transition Metal Dichalcogenides for Electrochemical Energy Conversion, *Adv. Mater.*, 2021, **33**(38), 2008376, DOI: 10.1002/adma.202008376.

23 X. Chia, A. Y. S. Eng, A. Ambrosi, S. M. Tan and M. Pumera, Electrochemistry of Nanostructured Layered Transition-Metal Dichalcogenides, *Chem. Rev.*, 2015, **115**(21), 11941–11966, DOI: 10.1021/acs.chemrev.5b00287.

24 S. M. Tan, Z. Sofer, J. Luxa and M. Pumera, Aromatic-Exfoliated Transition Metal Dichalcogenides: Implications for Inherent Electrochemistry and Hydrogen Evolution, *ACS Catal.*, 2016, **6**(7), 4594–4607, DOI: 10.1021/acscatal.6b00761.

25 L. Feng, W. Jiang, J. Su, L. Zhou and Z. Liu, Performance of Field-Effect Transistors Based on NbxW1−xS2 Monolayers, *Nanoscale*, 2016, **8**(12), 6507–6513, DOI: 10.1039/C6NR00380J.

26 Z. Qin, L. Loh, J. Wang, X. Xu, Q. Zhang, B. Haas, C. Alvarez, H. Okuno, J. Z. Yong, T. Schultz, N. Koch, J. Dan, S. J. Pennycook, D. Zeng, M. Bosman and G. Eda, Growth of Nb-Doped Monolayer WS2 by Liquid-Phase Precursor Mixing, *ACS Nano*, 2019, **13**(9), 10768–10775, DOI: 10.1021/acsnano.9b05574.

27 L. Tang, J. Tan, H. Nong, B. Liu and H.-M. Cheng, Chemical Vapor Deposition Growth of Two-Dimensional Compound Materials: Controllability, Material Quality, and Growth Mechanism, *Acc. Mater. Res.*, 2021, **2**(1), 36–47, DOI: 10.1021/accountsmr.0c00063.

28 M. Chhowalla, H. S. Shin, G. Eda, L.-J. Li, K. P. Loh and H. Zhang, The Chemistry of Two-Dimensional Layered Transition Metal Dichalcogenide Nanosheets, *Nat. Chem.*, 2013, **5**(4), 263–275, DOI: 10.1038/nchem.1589.

29 H. Jin, C. Guo, X. Liu, J. Liu, A. Vasileff, Y. Jiao, Y. Zheng and S.-Z. Qiao, Emerging Two-Dimensional Nanomaterials for Electrocatalysis, *Chem. Rev.*, 2018, **118**(13), 6337–6408, DOI: 10.1021/acs.chemrev.7b00689.

30 S. Bianchi, M. Bortoluzzi, V. Castelvetro, F. Marchetti, G. Pampaloni, C. Pinzino and S. Zacchini, The Reactivity of Tungsten Hexachloride with Tetrahydrofuran and 2-Methoxyethanol, *Polyhedron*, 2016, **117**, 769–776, DOI: 10.1016/j.poly.2016.07.024.

31 R. He, S. Lee, Y. Ding, C. Huang, X. Lu, L. Zheng, A. Yu, C. Zhang, C. Li, X. Bi, Y. Li, Y. Liao, J. Li, A. Ostovari Moghaddam, S. Yernar, Y. Xu, M. Ibáñez, C. Zhang, L. Yang, Y. Zhou and A. Cabot, Amorphous High Entropy Alloy Nanosheets Enabling Robust Li–S Batteries, *Adv. Funct. Mater.*, 2026, **36**(5), e13859, DOI: 10.1002/adfm.202513859.

32 X. Zhao, Q. Di, M. Li, Q. Yang, Z. Zhang, X. Guo, X. Fan, K. Deng, W. Chen, J. Zhang, J. Fang and Z. Quan, Generalized Synthesis of Uniform Metal Nanoparticles Assisted with Tungsten Hexacarbonyl, *Chem. Mater.*, 2019, **31**(12), 4325–4329, DOI: 10.1021/acs.chemmater.9b00219.

33 R. D. Shannon, Revised Effective Ionic Radii and Systematic Studies of Interatomic Distances in Halides and Chalcogenides, *Acta Crystallogr., Sect. A*, 1976, **32**(5), 751–767, DOI: 10.1107/S0567739476001551.

34 K. Fan, M. Shi, H. Li, Z. Xiang and X. Chen, Two-Dimensional Superconductivity in New Niobium Dichalcogenides-Based Bulk Superlattices, *Phys. Rev. Mater.*, 2025, **9**(3), 034804, DOI: 10.1103/PhysRevMaterials.9.034804.

35 W. Chen, G. Qian, H. Wang, D. Chen, X. Zhou, W. Yuan and X. Duan, Rationalizing the D-Band Model from Theory to Practice in Catalyst Design, *J. Am. Chem. Soc.*, 2025, **147**(51), 46729–46744, DOI: 10.1021/jacs.5c17673.

36 N. Kapuria, N. N. Patil, A. Sankaran, F. Laffir, H. Geaney, E. Magner, M. Scanlon, K. M. Ryan and S. Singh, Engineering Polymorphs in Colloidal Metal Dichalcogenides: Precursor-Mediated Phase Control, Molecular Insights into Crystallisation Kinetics and Promising Electrochemical Activity, *J. Mater. Chem. A*, 2023, **11**(21), 11341–11353, DOI: 10.1039/D2TA09892J.

37 Q. Ma and R. A. Rosenberg, Angle-Resolved X-Ray Photoelectron Spectroscopy Study of the Oxides on Nb Surfaces for Superconducting r.f. Cavity Applications, *Appl. Surf. Sci.*, 2003, **206**(1), 209–217, DOI: 10.1016/S0169-4332(02)01238-2.